(Received 25 July 2026, Accepted 31 August 2026, Scheduled 9 September 2026)

A Frequency-Selective Transmissive/Reflective Metasurface for Polarization Conversion in the V-Band

Mudrik Alaydrus*, Defi Lestari, Said Attamimi, and Umaisaroh

Department of Electrical Engineering, Universitas Mercu Buana, Jakarta, Indonesia

ABSTRACT: This study presents a compact frequency-selective metasurface for transmissive and reflective polarization conversion over the V-band (40–65 GHz). The structure consists of two Rogers RO4003C substrates separated by a 0.2-mm air gap and interconnected by a metallic post to enhance electromagnetic coupling. We performed parametric optimization to obtain multiple polarization-conversion bands. The optimized unit cell has a periodicity of 3.9 mm and employs resonator dimensions of $L_1 = 2.6\,\text{mm}$, $L_2 = 2.1\,\text{mm}$, $W = 1.0\,\text{mm}$, $S = 0.3\,\text{mm}$, $H = 0.2\,\text{mm}$, and $D = 0.3\,\text{mm}$. We conducted full-wave simulations and free-space measurements using WR-19 horn antennas and a vector network analyzer for validation. The proposed structure exhibits frequency-selective polarization-conversion behavior, with the transmission conversion exceeding 90% over approximately 40–49 GHz and near-unity conversion at selected frequencies, while the reflection conversion approaches 100% at resonant frequencies of approximately 58 and 60.5 GHz. The fabricated prototype showed good agreement with simulations, with minor discrepancies attributed to fabrication and measurement uncertainties. The proposed structure is promising for millimeter-wave communications, intelligent electromagnetic surfaces, radar sensing, transmitarray antennas, and future 6G systems.

1. INTRODUCTION

The polarization of an electromagnetic (EM) wave is defined by the orientation of its electric field vector, which is orthogonal to the direction of the wave propagation. Polarization, as one of the fundamental characteristics of electromagnetic waves, plays a vital role in determining the performance of wireless communication, radar, and sensing systems. The interaction of an EM wave with materials and receiving antennas is strongly influenced by its polarization state, directly affecting transmission efficiency, signal integrity, and system reliability [1]. Consequently, the ability to manipulate electromagnetic polarization has become increasingly important in modern microwave and millimeter-wave technologies. Various polarization-control devices, including polarizers and polarization converters, have been developed to tailor the polarization state of incident waves. Among them, metasurfaces have emerged as a promising solution because of their capability to manipulate electromagnetic waves with high flexibility in both reflection and transmission modes [2]. A metasurface is a two-dimensional artificial structure composed of periodically arranged subwavelength metallic and/or dielectric elements that enables precise control of the amplitude, phase, and polarization of electromagnetic waves.

Previous studies have shown that transmissive polarization converters generally suffer from relatively narrow operating bandwidths because their performance relies primarily on resonant electromagnetic responses. In contrast, reflective polarization converters can achieve considerably broader bandwidths via anisotropic phase manipulation and control the reflection characteristics [3]. Consequently, extensive research has focused on developing reflective polarization-conversion metasurfaces.

Several broadband and compact metasurfaces have been reported for reflective linear-to-linear (LP-to-LP) polarization conversion. A broadband anisotropic reflective metasurface was introduced in [4], while a reconfigurable design employing PIN diodes achieved broadband operation with a high polarization conversion ratio (PCR) through electronic control [5]. Compact dual-band implementations based on dual split-ring resonators and cut-wire structures were proposed in [6] and [7], demonstrating efficient LP-to-LP polarization conversion with relatively simple geometries. More recently, a bi-layer reflective metasurface achieving PCR greater than 80% under extremely wide incident angles up to $\pm 80^\circ$ was presented in [8], highlighting the potential for wide-angle polarization conversion.

In addition to LP-to-LP conversion, significant efforts have been devoted to linear-to-circular (LP-to-CP) polarization conversion. A dual-band reflective metasurface utilizing elliptical frequency-selective surface (FSS) elements was reported in [9], providing nearly 100% PCR, equivalent-circuit validation and stable performance under incident angles approaching 90°. An ultra-wideband reflective polarization converter employing double V-shaped and split-ring resonators was proposed in [10], simultaneously achieving PCR above 90% over 7.1–22.3 GHz and substantial radar cross-section reduction. Similarly, an FSS-backed reflective polarization converter designed for stealth radomes demonstrated low-loss transmission in the

* Corresponding author: Mudrik Alaydrus (mudrikalaydrus@mercubuana.ac.id).

doi:10.2528/PIERM26072504

operating band while providing broadband cross-polarized reflection over a much wider frequency range [11].

To further enhance their functionality, researchers have developed multiband and multifunctional reflective metasurfaces. Representative examples include a quad-band reflective metasurface for LP-to-CP conversion with excellent angular stability [12], a multifunctional reflective metasurface capable of dual-band cross-polarization and broadband LP-to-CP conversion [13], and a dual-band reflective polarization converter that simultaneously supports LP-to-LP conversion together with discrete LP-to-CP conversion at four operating frequencies [14]. These studies demonstrate that integrating multiple polarization-conversion mechanisms within a single reflective structure is an important research direction.

Substantial progress has also been achieved in transmissive polarization converters. A three-layer transmissive metasurface reported in [15] achieved a PCR exceeding 95% over the C-, X-, and Ku-bands with an impressive 105% fractional bandwidth and experimental validation. Likewise, an ultrathin anisotropic metasurface designed for 6G applications demonstrated a 98% PCR, high transmission efficiency, and a compact unit-cell configuration [16]. These studies confirm that high-efficiency transmissive polarization conversion is feasible, although its bandwidth remains largely constrained by resonance-based operations.

Recently, increasing attention has been directed toward simultaneous reflective-transmissive polarization converters, which provide different electromagnetic functionalities in different frequency bands. A bifunctional metasurface based on complementary S-shaped structures was proposed in [17], enabling independent transmissive and reflective linear-polarization conversion. Similar concepts were further explored through a dual-band polarization rotator with independently controlled transmission and reflection modes [18], an ultrathin single-layer converter with independently tunable transmission and reflection bands [19], and a reconfigurable three-layer metasurface employing only a single PIN diode to realize seven distinct transmission and reflection operating modes [20]. These multifunctional designs significantly improve the flexibility of polarization manipulation while maintaining a compact structural configuration.

Beyond conventional anisotropic structures, bi-anisotropic metasurfaces have recently attracted considerable attention owing to their capability to simultaneously control reflection and transmission characteristics. For instance, the omega bi-anisotropic metasurface reported in [21] achieved a 67.9% reflective polarization-conversion bandwidth, low-loss bandpass transmission, dual circular-polarization bands, and asymmetric reflection using only a two-layer configuration.

Despite these advances, existing polarization converters face several limitations. Most designs support only a single polarization conversion function or operate exclusively in either the reflection or transmission mode. Although multifunctional metasurfaces have been reported, they often rely on multilayer structures, active components, or complicated unit-cell geometries, resulting in increased fabrication complexity and insertion loss. Therefore, developing a compact passive metasurface capable of simultaneously providing efficient reflective and transmissive polarization conversions over the V-band remains an important research challenge.

This work extends our previous study in [22] by developing a frequency-selective metasurface capable of realizing both transmissive and reflective polarization conversion at different operating frequencies within the V-band. Unlike structures intended to provide simultaneous transmission and reflection over the same frequency range, the proposed configuration exploits the frequency-dependent coupling of its resonant elements to realize different polarization-conversion responses at different frequencies. Its electromagnetic performance was evaluated via full-wave simulations by analyzing both co-polarized and cross-polarized reflection and transmission characteristics. Experimental validation is carried out using a WR-19 waveguide measurement setup, and the measured results closely agree with the simulated predictions.

The proposed V-band polarization converter is particularly relevant to millimeter-wave communication systems in which polarization control is required to improve channel utilization, mitigate polarization mismatch, and support flexible electromagnetic-wave management. The broadband transmission/reflection characteristics of the proposed structure also make it potentially suitable for polarization-control components in high-frequency wireless front ends and emerging 6G communication systems. In such applications, a compact passive structure capable of manipulating the polarization state over a wide frequency range is attractive because it can provide additional electromagnetic functionality without requiring active tuning components or complex multilayer configurations.

2. UNIT CELL MODEL

Figure 1 illustrates the detailed geometry of the proposed metasurface unit cell. The structure consists of two identical dielectric substrates fabricated using Rogers RO4003C with a rela-

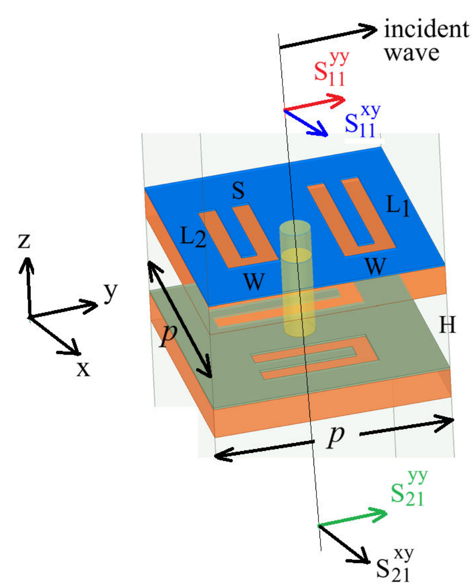

FIGURE 1. Detailed geometry of the metasurface unit cell.

tive permittivity of $\varepsilon_r = 3.38$, loss tangent $\tan\delta = 0.0027$, and thickness of 0.51 mm. The two substrates are separated by an air gap of height H, forming a multilayer configuration that provides additional degrees of freedom for controlling their electromagnetic response. Each substrate had a square periodicity of $p \times p$, which defined the lattice constant of the metasurface array. Metallic slot resonators are etched on both substrates. The upper layer consists of a pair of parallel slot resonators with lengths L_1 and L_2, slot width W, and spacing S. The lower layer employs the identical slot-resonator geometry as the upper layer but is rotated by 90°, forming an orthogonal configuration between the two metallic layers. The two layers are separated by an air gap of height H, while a metallic post with diameter D provides an electrical connection between corresponding metallic layers. The orthogonal arrangement of the identical resonators introduces anisotropic electromagnetic coupling and supports multiple resonant modes, contributing to the frequency-selective polarization-conversion response across the V-band.

Throughout this study, the incident wave is assumed y-polarized. The first and second superscripts of the scattering parameters denote the output and incident polarization states, respectively. Accordingly, S_{11}^{yy} and S_{21}^{yy} represent the co-polarized reflection and transmission coefficients, respectively, whereas S_{11}^{xy} and S_{21}^{xy} represent the cross-polarized reflection and transmission coefficients, respectively. Here, S_{11}^{xy} and S_{21}^{xy} describe the conversion of the incident y-polarized wave into the orthogonal x-polarized reflected and transmitted waves, respectively.

Then, the polarization conversion performance of the proposed metasurface is quantitatively evaluated using the Polarization Conversion Ratio (PCR), which represents the fraction of the total scattered electromagnetic power converted into the orthogonal polarization state. A higher PCR indicates a more efficient polarization conversion, whereas a lower value implies that the incident polarization is largely preserved.

For reflection mode, the reflected polarization conversion ratio is defined as

$$\mathrm{PCR_{ref}} = \frac{|S_{11}^{xy}|^2}{|S_{11}^{xy}|^2 + |S_{11}^{yy}|^2}. \tag{1}$$

A value of $\mathrm{PCR_{ref}} = 1$ (or 100%) indicates complete conversion of the reflected wave into orthogonal polarization, whereas $\mathrm{PCR_{ref}} = 0$ corresponds to purely co-polarized reflection. Similarly, the polarization conversion ratio for the transmitted wave is expressed as

$$\mathrm{PCR_{tr}} = \frac{|S_{21}^{xy}|^2}{|S_{21}^{xy}|^2 + |S_{21}^{yy}|^2}. \tag{2}$$

Therefore, the transmission PCR describes the efficiency with which the transmitted electromagnetic wave is converted from its original polarization to an orthogonal polarization state.

The structure is analyzed using the commercial software ANSYS HFSS, which employs the finite element method to discretize the geometry into small tetrahedral elements until convergence is attained. The simulation was performed across the frequency range of 40 GHz to 65 GHz, with 451 discrete frequency points.

3. RESULTS AND DISCUSSION

3.1. Unit-Cell Parametric Analysis

Following the initial unit-cell design, a comprehensive parametric study was carried out to investigate the influence of geometrical parameters on the electromagnetic response and to achieve the desired multiband polarization-conversion characteristics throughout the V-band. The study included systematic variations of the unit-cell periodicity (p), the lengths of the two slot resonators (L_1 and L_2), the slot width (W), the spacing between adjacent slots (S), the air-gap height between the two dielectric layers (H), and the diameter of the supporting metallic post (D).

Each parameter was independently optimized while keeping the remaining dimensions unchanged in order to evaluate its effect on resonant frequencies, impedance matching, bandwidth, and polarization conversion efficiency.

For clarity, the parametric analysis is divided into two groups: resonator dimensions (L_1 and L_2) and interlayer coupling parameters (D and H).

Figure 2 illustrates the influence of slot lengths L_1 and L_2 on the co-polarized reflection coefficient S_{11}^{yy}. It can be observed that both parameters significantly affect the resonant frequencies and impedance-matching characteristics of the proposed metasurface. As length L_1 increases, the first resonance shifts toward lower frequencies due to the increase in the effective electrical length of the resonator, which consequently reduces its resonant frequency. In contrast, variations in L_2 predominantly influence higher-order resonances, indicating that the second slot resonator primarily controls upper operating bands. Among the investigated dimensions, $L_1 = 2.6$ mm and $L_2 = 2.1$ mm provide the most favorable multiband response, producing well-defined resonance notches with improved impedance matching throughout the 40–65 GHz operating band. These results demonstrate that lower- and higher-frequency resonances can be independently tuned by adjusting L_1 and L_2, respectively. Such independent tuning capability provides greater design flexibility and facilitates metasurface optimization to achieve the desired multiband polarization conversion performance across the V band.

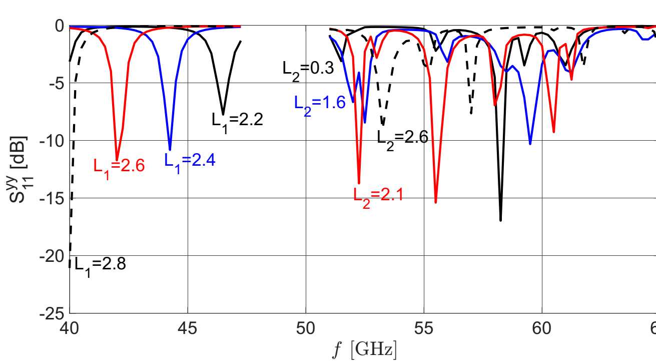

FIGURE 2. Reflected waves S_{11}^{yy} as function of the parameters L_1 and L_2.

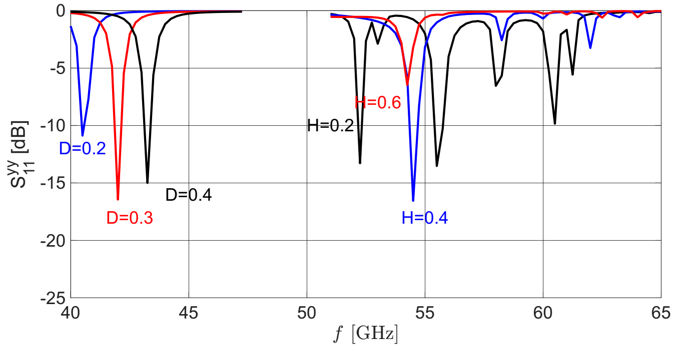

FIGURE 3. Reflected waves S_{11}^{yy} as function of the parameters D and H.

Figure 3 presents effects of the metallic-via diameter (D) and air-gap height (H) on the co-polarized reflection coefficient, S_{11}^{yy}. Both parameters play crucial roles in determining the resonance characteristics and impedance matching of the proposed metasurface. The diameter of the metallic via primarily affects the lower-frequency resonance by modifying the inductive coupling between the upper and lower resonators. As D increases, the effective inductance decreases, resulting in a shift in the resonant frequency and changes in the reflection magnitude. Among the investigated values, $D = 0.3$ mm provided the deepest resonance notch and the best impedance matching. By contrast, the air-gap height H governs the electromagnetic coupling strength between the two substrate layers. Increasing H weakens the near-field interaction, thereby shifting the resonant frequencies and reducing the resonance depth, whereas a smaller air gap enhances the interlayer coupling and promotes stronger field confinement in the device. The optimum value of $H = 0.2$ mm produces multiple well-defined resonances with superior impedance matching over the 40–65 GHz operating band. These results demonstrate that proper optimization of both the via diameter and air-gap height is essential for controlling the coupling mechanism and achieving the desired multiband polarization-conversion performance.

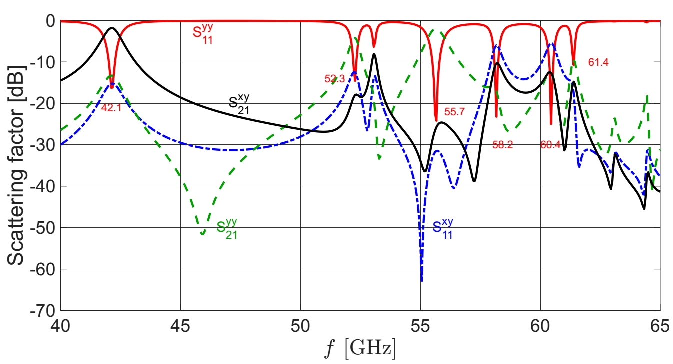

FIGURE 4. Reflected (S_{11}^{xy},S_{11}^{yy}) and transmitted (S_{21}^{xy} and S_{21}^{yy}) waves.

Based on the extensive parametric analysis, we obtained the optimum design with dimensions $p = 3.9$ mm, $L_1 = 2.6$ mm, $L_2 = 2.1$ mm, $W = 1.0$ mm, $S = 0.3$ mm, $H = 0.2$ mm, and $D = 0.3$ mm. We subsequently employed this optimized geometry in all numerical simulations and experimental validations presented in the following sections.

Figure 4 presents simulated reflection and transmission characteristics of the proposed metasurface for a y-polarized incident wave over the frequency range of 40–65 GHz. The reflection coefficients, represented by S_{11}^{yy} and S_{11}^{xy}, and the transmission coefficients, S_{21}^{yy} and S_{21}^{xy}, provide a comprehensive understanding of the polarization conversion mechanism. As observed, the co-polarized reflection coefficient (S_{11}^{yy}) remains close to 0 dB over most of the operating band, indicating that the structure predominantly operates in reflection mode. However, several pronounced resonant notches appeared at 42.1, 52.3, 55.7, 58.2, 60.4, and 61.4 GHz, where the reflected energy was significantly redistributed into other scattering channels. These resonant frequencies correspond to the excitation of different slot resonant modes supported by the multilayer metasurface.

The cross-polarized reflection coefficient (S_{11}^{xy}) exhibits deep minima, particularly around 55 GHz, indicating that only a small portion of the reflected wave is converted into the orthogonal polarization state. The transmission responses exhibited complementary behavior. The co-polarized transmission coefficient (S_{21}^{yy}) shows several resonance dips, confirming that the incident wave strongly interacts with the slot resonators and experiences frequency-selective transmission suppression. In contrast, the cross-polarized transmission coefficient (S_{21}^{xy}) exhibits several resonance peaks, particularly at 42, 53, 58, and 60 GHz, suggesting enhanced coupling between orthogonal field components at these frequencies.

Dielectric and conductor losses are explicitly included in all full-wave simulations. Rogers RO4003C substrates are modeled with a relative permittivity of $\varepsilon_r = 3.38$ and a loss tangent of $\tan\delta = 0.0027$, while all metallic elements, including the slot resonators and the connecting metallic post, are modeled as copper with finite electrical conductivity. Consequently, the simulated scattering parameters inherently account for dielectric and conductor losses. The transmission insertion loss associated with the cross-polarized transmission channel is evaluated as $IL = -20\,\lg_{10}|S_{21}^{xy}|$. Therefore, the reported simulated transmission response represents the performance of the proposed structure under lossy material conditions rather than an ideal lossless-material assumption.

Figure 5 shows the polarization conversion ratio (PCR) of the proposed metasurface for normal (0°) incidence in both reflection and transmission modes. The transmission PCR (blue curve) exhibits broadband polarization conversion from approximately 40 to 49 GHz, maintaining values above 0.9 with

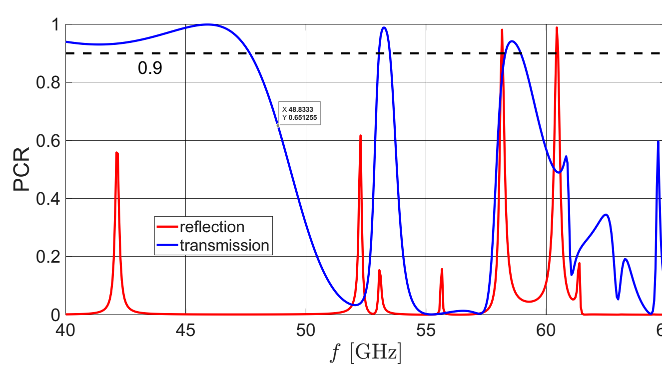

FIGURE 5. PCR characteristics for 0^o incident angle.

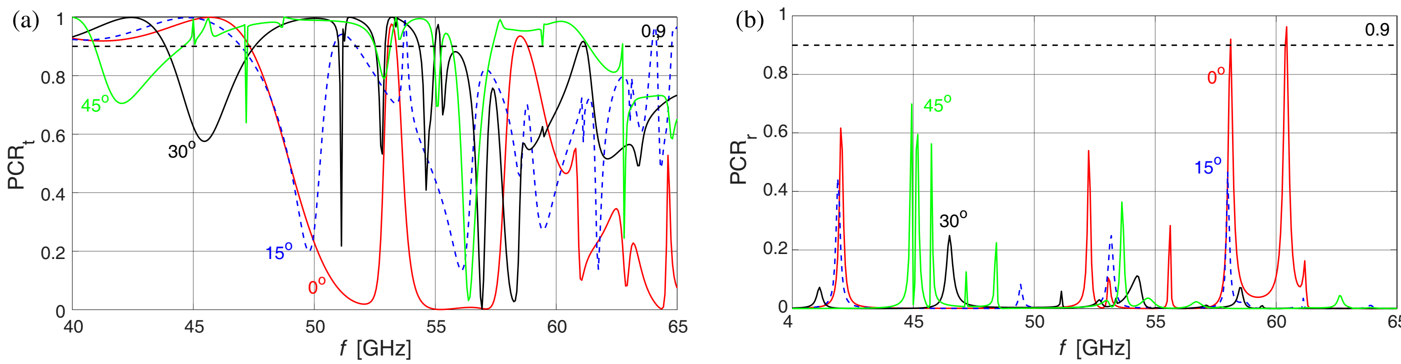

FIGURE 6. Calculated PCR characteristics for different incident angles. (a) Transmissive PCR and (b) reflective PCR.

a maximum approaching unity near 46 GHz. Additional high-efficiency transmission peaks were observed at approximately 53 GHz and 58–59 GHz. In contrast, the reflection PCR (red curve) is generally low over most of the operating band but reaches nearly 100% at discrete resonant frequencies of approximately 58 and 60.5 GHz. Results demonstrate that the proposed metasurface provides frequency-selective transmissive and reflective polarization conversion. In the lower portion of the V-band, the structure exhibits strong cross-polarized transmission, whereas at selected higher-frequency resonances, the response becomes reflection-dominant. Thus, the two functionalities are realized at different frequencies rather than simultaneously across the entire operating band.

Figure 6 compares the polarization conversion ratio (PCR) of the proposed metasurface at incident angles ranging from 0° to 45°. As shown in Fig. 6(a), the transmissive PCR remains above 0.9 in several operating bands for all incident angles, indicating that the proposed metasurface maintains stable polarization-conversion performance for incident angles up to 45°. For normal incidence (0°), high-transmission PCR is achieved from approximately 40 to 49 GHz, whereas increasing the incident angle gradually shifts the high-PCR regions toward higher frequencies. Nevertheless, even at an incident angle of 45°, the metasurface maintains PCR values exceeding 0.9 at several resonant frequencies, indicating that efficient polarization conversion is preserved at oblique incidence. In contrast, the reflective PCR shown in Fig. 6(b) exhibits relatively narrow-band resonant peaks that are more sensitive to the incident angle. The highest reflective PCR is obtained for normal incidence near 58–61 GHz, whereas increasing the incident angle generally reduces both resonance intensity and bandwidth. Overall, these results demonstrate that the proposed metasurface has good polarization-conversion stability in incident angles up to 45° in transmission while maintaining frequency-selective reflective polarization conversion, making it well suited for practical V-band applications where electromagnetic waves may impinge from different directions.

Figure 7 illustrates surface-current distributions on upper and lower metallic layers at the three principal resonant frequencies of 42.1, 55.7, and 60.4 GHz, providing insight into the underlying polarization-conversion mechanism. At 42.1 GHz, where the cross-polarized transmission coefficient (S_{21}^{xy}) reaches its maximum, the surface current is mainly concentrated along the

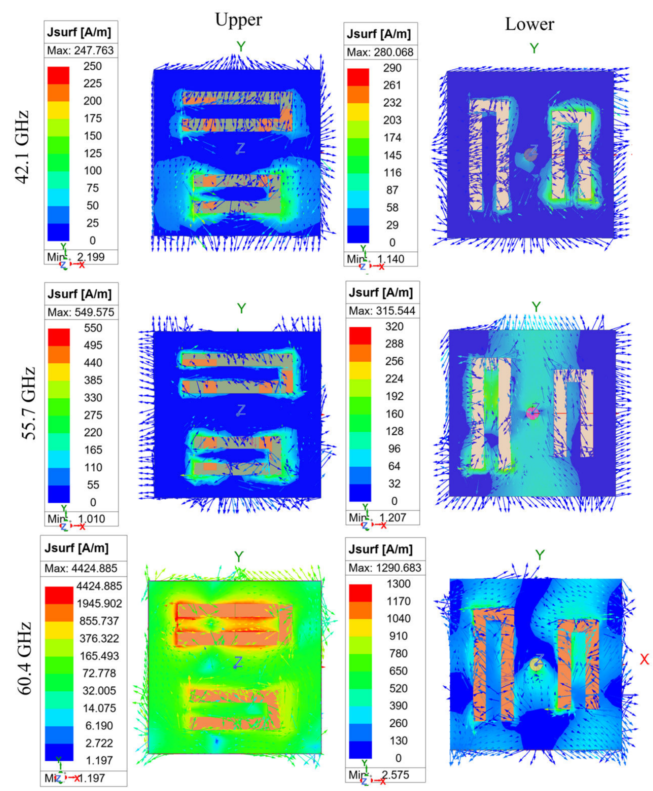

FIGURE 7. Surface current distribution on upper and lower metallic sides at resonant frequencies 42.1 GHz, 55.7 GHz, and 60.4 GHz.

slot edges of the upper resonator and is efficiently coupled to the lower resonator through the metallic via. The strong current confinement and complementary current paths in the two layers indicate efficient interlayer electromagnetic coupling, enabling the incident wave to convert into its orthogonal polarization while propagating through the metasurface.

At 55.7 GHz, corresponding to the maximum co-polarized transmission coefficient (S_{21}^{yy}), the current distribution is dominated by the upper resonator, and the lower layer shows a comparatively weaker excitation than the upper resonator. This configuration favors direct transmission with minimal polarization rotation, explaining the high co-polarized transmission observed at this frequency. The electromagnetic coupling remains sufficient to maintain impedance matching but is insufficient to induce a significant polarization conversion.

In contrast, at 60.4 GHz, where the cross-polarized reflection coefficient (S_{11}^{xy}) attains its highest value, intense surface currents are excited simultaneously on both metallic layers. The strong current circulation around the slot resonators and metallic via produces enhanced inductive and capacitive coupling, resulting in substantial field confinement within the structure. Consequently, the transmitted energy is significantly reduced, whereas the reflected wave is efficiently converted into an orthogonal polarization state. These current distributions confirm that the proposed dual-layer resonator supports different resonant modes, allowing the metasurface to selectively operate in transmissive or reflective polarization conversion, depending on the excitation frequency.

3.2. Full-Wave Simulation Setup

Figure 8 illustrates the full-wave simulation model used to characterize the proposed metasurface under free-space excitations. Two standard WR-19 rectangular waveguides operating in the V-band (40–65 GHz) were positioned on opposite sides of the metasurface with a separation distance of 80 mm. The metasurface consists of a 10×10 array of periodic unit cells printed on a dielectric substrate, resulting in an overall dimension of $39 \times 39 \times 2.445\,\text{mm}^3$. The array size was sufficiently large to minimize edge diffraction, allowing the calculated scattering parameters to closely approximate those of an infinite periodic structure.

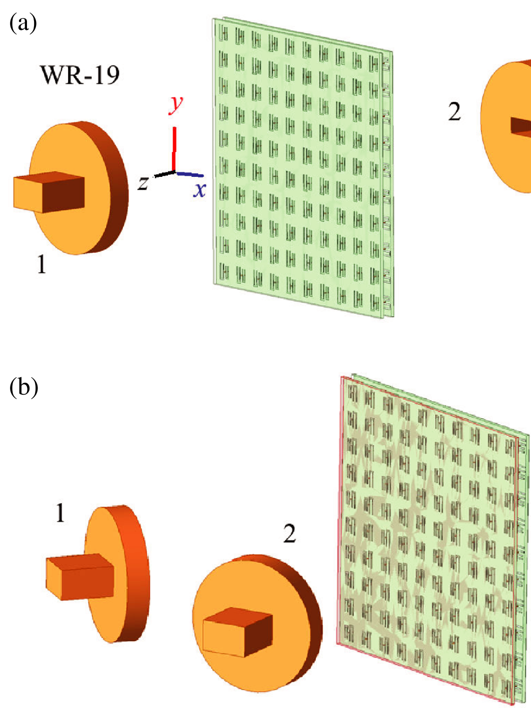

FIGURE 8. HFSS model for characterization of (a) transmission and (b) reflection properties of the designed metasurfaces.

As shown in Fig. 8(a), the first simulation configuration was employed to evaluate transmission characteristics. The transmitting WR-19 waveguide excited the dominant TE_{10} mode, generating an y-polarized electromagnetic wave that propagated toward the metasurface. The receiving waveguide was initially aligned with the transmitting waveguide to measure the co-polarized transmission coefficient (S_{21}^{yy}). It was subsequently rotated by 90° to measure the cross-polarized transmission coefficient (S_{21}^{xy}).

The second configuration, shown in Fig. 8(b), was used to characterize the reflection properties of the proposed metasurface. In this case, one WR-19 waveguide was rotated by 90° with respect to the other, enabling measurement of the cross-polarized reflection coefficient (S_{11}^{xy}). Together with the co-polarized reflection coefficient (S_{11}^{yy}), these scattering parameters are used to calculate the polarization conversion ratio (PCR).

The adopted simulation model closely followed the experimental measurement setup, ensuring consistent excitation conditions and enabling a direct comparison between simulated and measured results.

3.3. Fabrication and Measurement Setup

Figure 9 shows the fabricated reflective, transmissive metasurface polarization converter, which is composed of a periodic array of metallic resonators printed on a dielectric substrate. As shown in Figs. 9(a)–(b), the metallic posts were soldered after assembling the two substrate layers to establish electrical connections between the corresponding metallic surfaces. Fig. 9(c) shows the bottom side of the lower layer, while Fig. 9(d) provides a side view of the fabricated structure and clearly shows the metallic posts connecting the two layers.

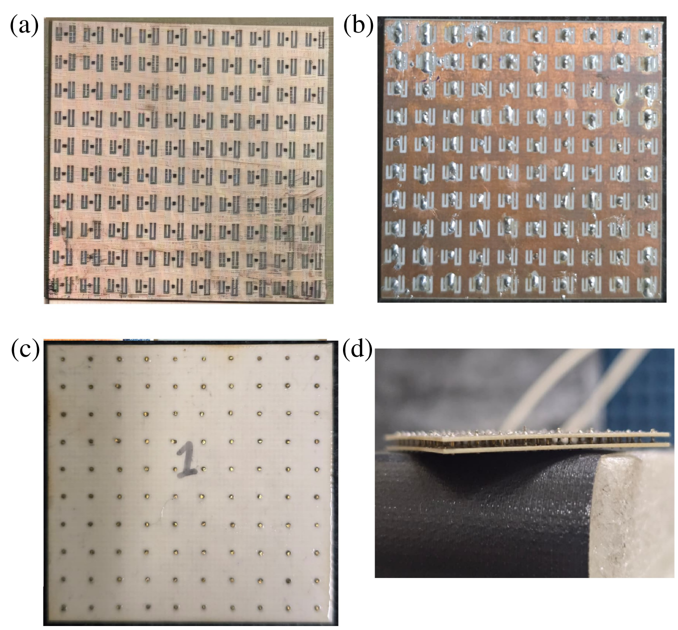

FIGURE 9. Fabricated transmissive-reflective polarization converter: (a) structure before soldering the metallic posts, (b) structure after soldering the metallic posts, (c) bottom view of the lower metallic layer, and (d) side view showing the metallic posts connecting the two layers.

According to the datasheet of RO4003C, the dielectric constant ranges in the interval 3.38 ± 0.05, and the thickness ranges from 0.4699 mm to 0.5461 mm. The etching accuracy was ± 0.05 mm, and the metallic post diameter was 0.3 mm ± 0.05 mm.

(a) (b) (c)

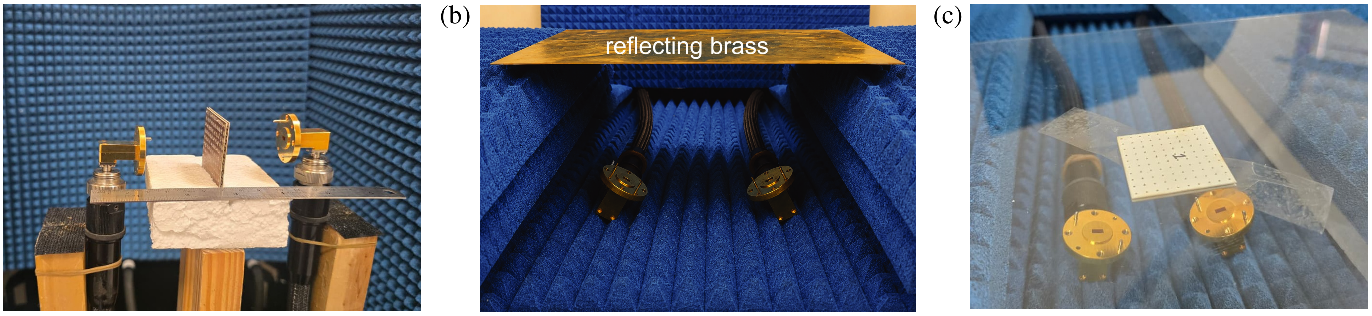

FIGURE 10. Photographs of the measurement setups used for the characterization of the proposed metasurface: (a) transmission measurement, (b) reflection measurement using a metallic reference plate, and (c) reflection measurement of the fabricated metasurface.

The metallic connection between upper and lower layers was realized using a conductive metal post with a nominal diameter of $D = 0.3\,\text{mm}$. The post was inserted through aligned holes in the two dielectric substrates and soldered to the corresponding metallic layers to ensure reliable electrical continuity. The soldered connection was subsequently inspected to ensure mechanical and electrical contact.

Figure 10(a) shows the experimental setup used to characterize the proposed metasurface polarization converter in the V-band frequency range. The measurement system consists of two WR-19 standard-gain horn (aperture) antennas connected to a vector network analyzer (VNA) R&S ZVA67 through suitable waveguide-to-coaxial adapters. The VNA was calibrated using the standard via reflect-line (TRL) calibration method for WR-19. The fabricated metasurface sample was positioned between the transmitting and receiving antennas and held vertically using a non-metallic wooden fixture to minimize unwanted scattering and reflections.

For the transmission coefficient measurement, one WR-19 antenna acted as the transmitter while the other functioned as the receiver. The transmitting antenna illuminates the metasurface with a linearly polarized electromagnetic wave, and the antennas are separated by 80 mm $\pm$ 0.5 mm. The receiving antenna, which was placed on the opposite side of the sample, captured the transmitted signal. Measured transmission parameters included both co-polarized and cross-polarized transmission coefficients. To obtain these quantities, the receiving antenna was rotated according to the desired polarization orientation. When both antennas had the same polarization orientation, the co-polarized transmission coefficient was measured, whereas a 90° rotation of the receiving antenna enabled measurement of the cross-polarized transmission coefficient.

Transmitting and receiving WR-19 apertures have dimensions of $4.7752 \times 2.3876\,\text{mm}^2$. The maximum aperture dimension is therefore $D_{ant} = 4.7752\,\text{mm}$. We evaluated the conventional far-field boundary using $R_{FF} = 2D_{ant}^2/\lambda$. Over the 40–65 GHz operating band, R_{FF} varies from approximately 6.08 mm at 40 GHz to 9.88 mm at 65 GHz. Since the horn-to-metasurface separation is 80 mm, the measurement distance is more than eight times the maximum far-field boundary calculated for the WR-19 aperture. Thus, the measurement satisfies the conventional far-field criterion with respect to the radiating aperture of the WR-19 antenna.

Nevertheless, because the fabricated metasurface has a finite aperture of $39 \times 39\,\text{mm}^2$, finite-distance illumination may introduce phase curvature across the sample. This effect was therefore considered in the sensitivity analysis by introducing variations in the measurement geometry and comparing the resulting responses with the nominal configuration. The results indicate that the principal spectral characteristics are preserved despite these practical variations.

To determine the reflection coefficient, the metasurface is illuminated by the transmitting antenna, and the reflected signal is measured using the receiving antenna placed on the same side of the sample or via an equivalent free-space reflection measurement configuration. Before measurement, a reference calibration is performed using a metallic plate of identical dimensions to establish the 0-dB reflection reference level, as shown in Fig. 10(b). The reflected response from the metasurface (Fig. 10(c)) was then normalized to this reference to obtain the reflection coefficient.

Microwave absorber panels surrounding the measurement region were employed to suppress unwanted reflections from nearby objects and the laboratory environment, improving measurement accuracy. The separation distance between antennas and the metasurface was selected to satisfy the far-field conditions. The VNA records scattering parameters over the frequency range of interest, from which reflection and transmission coefficients are extracted and compared with simulated results.

3.4. Simulated and Measured Results

Figure 11 compares simulated and measured co-polarized transmission coefficiens (S_{21}^{yy}) of the proposed metasurface in the 40–65 GHz frequency range. Without the metasurface, both the simulated and measured responses remained approximately between -28 and -34 dB, indicating stable free-space transmission. After inserting the metasurface, S_{21}^{yy} was reduced by approximately 20–30 dB, confirming strong suppression of the original polarization. Measured results closely follow simulated trends, with minor discrepancies attributed to fabrication tolerances, waveguide alignment, calibration uncertainty, and multiple reflections commonly encountered in millimeter-wave measurements.

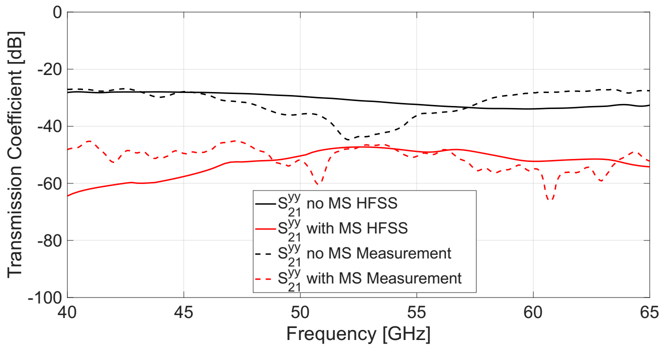

FIGURE 11. Calculated and measured S_{21}^{yy} as function of frequency.

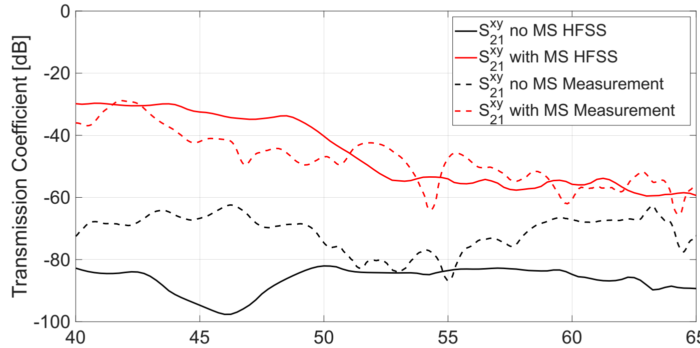

FIGURE 12. Calculated and measured S_{21}^{xy} as function of frequency.

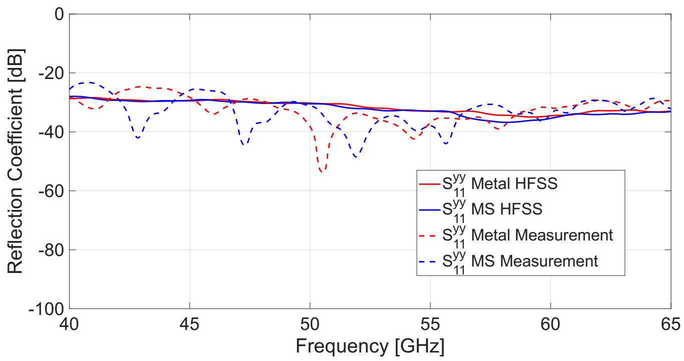

FIGURE 13. Calculated and measured S_{11}^{yy} as function of frequency.

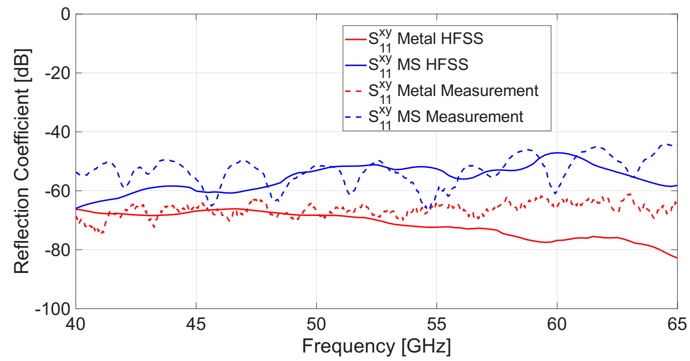

FIGURE 14. Calculated and measured S_{11}^{xy} as function of frequency.

Figure 12 presents simulated and measured cross-polarized transmission coefficients (S_{21}^{xy}). Without the metasurface, cross-polarized transmission is negligible throughout the operating band. Introducing the metasurface significantly increased S_{21}^{xy}, demonstrating efficient polarization conversion. Although the measured response exhibited additional resonant fluctuations, particularly near 46, 54, 60, and 64 GHz, the overall agreement with simulations remained satisfactory. These differences are mainly caused by fabrication tolerances, variations in dielectric properties, and measurement uncertainties. In contrast to the co-polarized transmission shown in Fig. 11, the cross-polarized transmission is expected to increase when the metasurface is introduced, indicating that the incident electromagnetic wave is converted into its orthogonal polarization.

The measured response shows several narrow resonant dips, particularly near 46 GHz, 54 GHz, 60 GHz, and 64 GHz, which are not fully reproduced in the simulation. These differences are primarily attributed to fabrication tolerances, dielectric constant variations, conductor surface roughness, slight waveguide misalignment, flange discontinuities, and measurement uncertainties, which become increasingly significant at millimeter-wave frequencies. Despite these local deviations, measured characteristics were in good agreement with simulated results. Overall, the comparison between the reference and metasurface-loaded configurations clearly demonstrates the effectiveness of the proposed metasurface in enhancing cross-polarized transmission. When considered together with substantial suppression of the co-polarized transmission shown in Fig. 11, these results verify that the proposed structure successfully performs polarization conversion in the V-band. The close agreement between simulation and measurement further confirms the reliability of the design methodology and validates the electromagnetic performance of the fabricated metasurface.

Figure 13 compares simulated and measured co-polarized reflection coefficients (S_{11}^{yy}) for both the metallic reference and the proposed metasurface. The simulated responses remained below approximately -28 dB across the V-band, whereas the measured results exhibited additional narrow resonances caused by fabrication and measurement imperfections. Despite these fluctuations, both the simulation and measurement results demonstrate good impedance matching and consistent reflection characteristics, confirming the validity of the proposed design.

Figure 14 shows simulated and measured cross-polarized reflection coefficients (S_{11}^{xy}). Both simulated and measured responses remained below approximately -45 dB throughout the operating band, indicating effective suppression of the undesired cross-polarized reflection. Although the measured results contain larger ripples than the simulations, mainly due to alignment errors and fabrication tolerances, the overall trends agree well, thus validating the predicted electromagnetic performance of the proposed metasurface.

Compared with Fig. 13, Fig. 14 demonstrates substantially lower reflection levels for both simulated and measured responses, confirming that the proposed structure effectively suppresses cross-polarized reflected fields while preserving broadband impedance matching. Although the measured S_{11}^{xy}

TABLE 1. Comparison of the proposed metasurface with recently reported polarization converters.

Ref.	Unit Cell Dimensions ($\lambda_0 \times \lambda_0$)	Type	Thickness (λ_0)	Operating Bandwidth (GHz)	Metallic Layers	PCR (%)	$\|T\|$	Polarization Conversion
[4]	0.41×0.41	Reflective	0.14	18.9–51.0	2	> 90	–	LP→LP
[5]	0.193×0.193	Reflective	0.0852	6.03–10.5	2	≥ 90	–	LP→LP
[6]	0.126×0.126	Reflective	0.057	5.4–9.0, 14.6–16.1	2	$\geq 93, \geq 90$	–	LP→LP
[7]	0.150×0.150	Reflective	0.065	9.8–15.1, 19.2–25.7	2	> 90	–	LP→LP
[8]	0.336×0.336	Reflective	0.035	5.04	3	> 80	–	LP→LP
[9]	0.35×0.35	Reflective	0.041	7.6–7.76, 9.27–9.57	2	99.9	–	LP→CP
[10]	0.50×0.50	Reflective	0.195	7.1–22.3	2	> 90	–	LP→LP
[11]	0.53×0.53	Reflective	0.16	7.0–17.6	4	> 95	–	LP →LP
[12]	0.30×0.30	Reflective	0.05	Quad-band (9.5–32.1)	2	> 90	–	LP→CP
[13]	0.20×0.20	Reflective	0.09	Penta-band (5.3–19.7)	3	> 90	–	LP→CP
[14]	0.225×0.225	Reflective	0.085	6.75–10.59, 17.78–19.61	2	≈ 100	–	LP→LP/CP
[15]	0.17×0.17	Transmissive	0.12	4.6–14.8	3	> 95	0.95	LP→LP
[16]	0.15×0.15	Transmissive	0.015	6.4–8.4	1	98	0.98	LP→LP
[17]	0.19×0.19	T/R	0.071	7.1–7.5(T), 16.6–16.9(R)	2	67(T), 83(R)	0.81	LP→LP
[18]	0.50×0.50	T/R	0.162	7.67–7.87(R), 9.25–9.54(T)	4	> 80	0.91	LP→LP
[19]	0.41×0.41	T/R	0.094	4.06–4.46(T), 6.04–8.31(R)	2	> 98	0.9	LP→LP
[20]	0.35×0.35	T/R	0.82	Triband (5.9–9.8)	3	>90	0.80	LP→LP/CP
[21]	0.33×0.33	T/R	0.18	Quadband (6.9–16.37)	2	89(R), 50(T)	0.94	LP→LP/CP
This work	$\mathbf{0.4350 \times 0.4350}$	**T/R**	**0.2775**	**Six-Band (40-65)**	**2**	$\mathbf{> 90}$	$\mathbf{> 0.90}$	**LP→LP**

responses exhibit greater ripple than the simulated results, the overall agreement remains satisfactory, and the average reflection characteristics closely follow the predicted trends. The consistently low cross-polarized reflection coefficients, together with the excellent co-polarized reflection performance observed in Fig. 13, verify the robustness of the proposed metasurface design and confirm its suitability for broadband V-band polarization conversion applications with minimal reflection loss.

3.5. Sensitivity Analysis and Simulation-Measurement Uncertainty

To further investigate the discrepancies between calculated and measured responses, a sensitivity analysis was performed by considering practical variations in geometrical, material, and measurement parameters. This analysis is motivated by the fabrication and measurement tolerances associated with the proposed V-band metasurface. In particular, the geometrical dimensions were varied within ± 0.05 mm, a small variation in the relative alignment of the transmitting and receiving waveguides was introduced, and the relative dielectric permittivity was varied by approximately $\pm 10\%$ from its nominal value. These perturbations were considered to represent the combined effects of fabrication tolerances, uncertainty in dielectric properties, and practical waveguide-alignment errors.

Figure 15 presents the resulting sensitivity analysis for the cross-polarized transmission coefficient S_{21}^{xy}. The solid curves represent the mean calculated response obtained from the perturbed models, while the shaded regions indicate the corresponding mean $\pm$ one standard deviation. Nominal calculated and measured responses are also included for direct comparison.

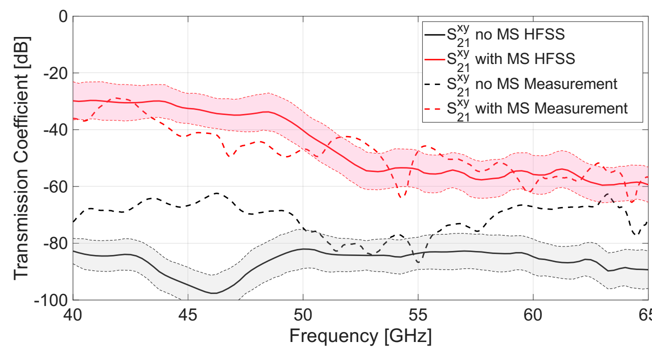

FIGURE 15. Sensitivity analysis of S_{21}^{xy} based on perturbed full-wave simulations with geometrical variations of ± 0.05 mm, waveguide-alignment variations, and approximately $\pm 10\%$ variation in relative dielectric permittivity. Solid curves represent the mean simulated responses, and shaded regions indicate the mean ± one standard deviation; dashed curves represent the measured responses.

Perturbed simulations exhibit variations around the nominal calculated response over the investigated 40–65 GHz frequency range. Nevertheless, the principal spectral characteristics and overall frequency-dependent trend remain preserved. The measured response generally follows the trend of the perturbed simulations and falls within or near the predicted variation range over a substantial portion of the operating band. This observation indicates that fabrication tolerances, dielectric-property variations, and waveguide alignment can contribute significantly to local differences between nominal full-wave simulations and experimental measurements.

These results provide additional evidence that observed simulation-measurement discrepancies do not necessarily originate from limitations of the proposed electromagnetic design, but can be reasonably associated with practical uncertainties inherent to millimeter-wave fabrication and measurement. Therefore, the sensitivity analysis provides a more quantitative assessment of the robustness of the proposed metasurface and supports the overall agreement between the calculated and measured results.

3.6. Comparison with Recent Works

Table 1 compares the proposed metasurface with representative reflective, transmissive, and transmissive/reflective polarization converters reported in the literature. The proposed unit cell has a normalized size of $0.435\lambda_0 \times 0.435\lambda_0$, which is larger than several reported designs. This larger footprint represents a deliberate trade-off for integrating transmissive and reflective polarization-conversion functionalities within a passive two-layer structure. The available area enables implementating multiple coupled slot resonators and their associated electromagnetic interactions. Despite the relatively larger unit-cell size, the proposed structure achieves broadband V-band operation, high polarization-conversion efficiency, and dual transmissive/reflective functionalities without active components or additional metallic layers.

4. CONCLUSION

We have presented, fabricated, and experimentally validated a compact dual-layer frequency-selective metasurface for transmissive and reflective polarization conversion in the V-band. The proposed structure employs coupled slot resonators separated by an air gap and interconnected through a metallic post, enabling a strong electromagnetic coupling and the excitation of multiple resonant modes. The optimized configuration has a unit-cell periodicity of $p = 3.9\,\text{mm}$, with $L_1 = 2.6\,\text{mm}$, $L_2 = 2.1\,\text{mm}$, $W = 1.0\,\text{mm}$, $S = 0.3\,\text{mm}$, $H = 0.2\,\text{mm}$, and $D = 0.3\,\text{mm}$. A systematic parametric investigation demonstrated that the geometrical dimensions of the resonators and their relative configuration significantly influence the resonance frequencies, impedance matching, and polarization-conversion characteristics.

The results demonstrate that the same passive structure can realize transmission-dominant polarization conversion over selected frequency regions and reflection-dominant polarization conversion at other resonant frequencies. We evaluated electromagnetic performance using full-wave HFSS simulations and experimentally verified with a free-space measurement setup based on WR-19 horn antennas. Measured results generally follow simulated characteristics, with discrepancies attributed to fabrication tolerances, dielectric-property variations, waveguide alignment, and measurement uncertainty. The additional sensitivity analysis further demonstrates the robustness of the predicted response to practical variations in the geometrical and material parameters.

The combination of broadband V-band operation, passive two-layer construction, compact unit-cell dimensions, and polarization-control capability makes the proposed structure a promising candidate for polarization-management components in millimeter-wave communication systems and emerging high-frequency wireless/6G front ends.

ACKNOWLEDGEMENT

This research was supported by the Directorate of Research and Community Service (DPPM), Ministry of Higher Education, Science, and Technology (Kemdiktisaintek), Republic of Indonesia, under the Penelitian Fundamental Regular Research Grant program No. 0988/LL3/AL.04/2025; 01-1-4/032/SPK-RISET/VI/2025 for the fiscal year 2025.

REFERENCES

[1] Stutzman, W. L., *Polarization in Electromagnetic Systems*, 2nd ed., Artech House, Norwood, MA, USA, 2018.

[2] Zhu, Q., H. Tian, and W. Jiang, "Manipulations and applications of radiating waves using electromagnetic metasurfaces," *Opto-Electronic Engineering*, Vol. 50, No. 9, 230115, 2023.

[3] Omar, A. A., "Reflective and transmissive linear polarization rotators: A review," *IEEE Open Journal of Antennas and Propagation*, Vol. 6, No. 3, 633–644, 2025.

[4] Zhang, B. and X. Liu, "Broadband efficient reflective linear polarization converter," *Progress In Electromagnetics Research C*, Vol. 159, 235–242, 2025.

[5] Neema, K. and D. D. Krishna, "Dual split ring resonator based reconfigurable reflective metasurface for linear-to-linear polarization conversion," *Progress In Electromagnetics Research M*, Vol. 124, 11–17, 2024.

[6] Kamal, B., J. Chen, Y. Yin, J. Ren, S. Ullah, and U. Ali, "Design and experimental analysis of dual-band polarization converting metasurface," *IEEE Antennas and Wireless Propagation Letters*, Vol. 20, No. 8, 1409–1413, 2021.

[7] Li, F., L. Zhang, P. Zhou, H. Chen, R. Zhao, Y. Zhou, D. Liang, H. Lu, and L. Deng, "Dual-band reflective polarization converter based on slotted wire resonators," *Applied Physics B*, Vol. 124, No. 2, 28, 2018.

[8] Wu, Y., S. Jia, and T. Zheng, "Design of an ultra-wide-angle reflective polarization conversion metasurfaces," in *2022 International Conference on Microwave and Millimeter Wave Technology (ICMMT)*, 1–3, Harbin, China, 2022.

[9] Madheswaran, S. and R. Venkatesan, "A dual-band reflective polarizer based meta-surface with higher angular stability for C and X-band applications," *Scientific Reports*, Vol. 14, No. 1, 29353, 2024.

[10] Ren, X., Y. Liu, Z. Ji, Q. Zhang, and W. Cao, "Ultra-wideband passive polarization conversion metasurface for radar cross-section reduction across C-, X-, Ku-, and K-bands," *Micromachines*, Vol. 16, No. 3, 292, 2025.

[11] Yan, M., J. Wang, W. Wang, C. Xu, H. Chen, W. Wang, L. Zheng, and S. Qu, "An FSS-backed reflective polarization conversion meta-surface for radar stealth," *Photonics and Nanostructures — Fundamentals and Applications*, Vol. 43, 100846, 2021.

[12] Eldesouki, E. M., S. M. El-Nady, S. A. M. Soliman, and A. M. Attiya, "Quad-band reflective metasurface for linear to circular polarization conversion," *Microwave and Optical Technology Letters*, Vol. 66, No. 6, e34223, 2024.

[13] Zhang, B., Q. Xie, T. Gao, S. Liu, and F. Xu, "A low-profile wide-angle multiband multifunctional reflective polarization conversion metasurface," *Microwave and Optical Technology Letters*, Vol. 67, No. 4, e70194, 2025.

[14] Lin, X., X. Zhang, M. Chang, W. Li, S. Yu, and M. Zhang, "Dual-band reflective polarization converter based on metasurface," *Optoelectronics Letters*, Vol. 19, No. 12, 716–720, 2023.

[15] Chandra, M., Nilotpal, D. Samantaray, M. Thottappan, and S. Bhattacharyya, "A broadband transmissive type metasurface

cross-polarization converter for EMC application," *IEEE Transactions on Electromagnetic Compatibility*, Vol. 65, No. 1, 186–194, 2023.

[16] Bose, M. and V. Karuppiah, "Design and experimental characterization of an anisotropic transmissive metasurface for polarization conversion in upper mid-band 6G systems," *Measurement*, Vol. 269, 120797, 2026.

[17] Shen, Z., Q. Zhang, X. Huang, J. Wu, and H. Yang, "Simultaneous transmissive and reflective polarization conversion cross different operating bands in a single metasurface," *Optics & Laser Technology*, Vol. 169, 110071, 2024.

[18] El Yousfi, A., J. M. Al-Ahmadi, A. M. A. Ahmed, and A. A. Omar, "Simple dual-band polarization rotator with independent control of transmissive and reflective modes," *Progress In Electromagnetics Research Letters*, Vol. 129, 42–46, 2026.

[19] Wan, H., G. Ding, L. Zhang, X. Luo, and S. Wang, "An ultrathin single-layer polarization converter with independently tunable transmission and reflection operating frequencies," *IEEE Antennas and Wireless Propagation Letters*, Vol. 25, No. 5, 2045–2049, 2026.

[20] Yang, H., Y. He, M. S. Tong, L. T. Guo, P. Li, and Y. J. Zhang, "A reflection-transmission multifunctional polarization conversion metasurface," *IEEE Transactions on Antennas and Propagation*, Vol. 72, No. 6, 5099–5109, 2024.

[21] Nasir, M., S. Koziel, and A. Pietrenko-Dabrowska, "A multifunctional bi-anisotropic metasurface with reflection-transmission polarization conversion and narrow bandpass transmission characteristics," *Scientific Reports*, Vol. 16, No. 1, 13838, 2026.

[22] Lestari, D., D. W. Astuti, U. Umaisaroh, N. A. Murad, and M. Alaydrus, "Transmissive dual-band polarization converter based on metal-only metasurface at V-band," in *2025 12th International Conference on Electrical Engineering, Computer Science and Informatics (EECSI)*, 194–197, Semarang, Indonesia, 2025.